Epsilon-Near-Zero Modes for Tailored Light-Matter Interaction

Salvatore Campione,[1,2,*] Sheng Liu,[1,2] Alexander Benz,[1,2] John F. Klem,[1] Michael B. Sinclair,[1] and Igal Brener[1,2,†]

[1]*Sandia National Laboratories, Albuquerque, New Mexico 87185, USA*

[2]*Center for Integrated Nanotechnologies (CINT), Sandia National Laboratories, Albuquerque, New Mexico 87185, USA*

(Received 17 February 2015; revised manuscript received 31 July 2015; published 20 October 2015)

Epsilon-near-zero (ENZ) modes arising from condensed-matter excitations such as phonons and plasmons are a new path for tailoring light-matter interactions at the nanoscale. Complex spectral shaping can be achieved by creating such modes in nanoscale semiconductor layers and controlling their interaction with multiple, distinct, dipole resonant systems. Examples of this behavior are presented at midinfrared frequencies for ENZ modes that are strongly coupled to metamaterial resonators and *simultaneously* strongly coupled to semiconductor phonons or quantum-well intersubband transitions (ISTs), resulting in double- and triple-polariton branches in transmission spectra. For the double-polariton branch case, we find that the best strategy to maximize the Rabi splitting is to use a combination of a doped layer supporting an ENZ feature and a layer supporting ISTs, with overlapping ENZ and IST frequencies. This design flexibility renders this platform attractive for low-voltage tunable filters, light-emitting diodes, and efficient nonlinear composite materials.

DOI: 10.1103/PhysRevApplied.4.044011

I. INTRODUCTION

The pursuit of natural and artificial epsilon-near-zero (ENZ) response has led to intriguing optical properties [1], including supercoupling [2–4], highly directional beaming [5–8], optical nanocircuits [9], optical switching and bistability [10,11], and cloaking devices [12]. In this work, we aim to tailor light-matter interactions at the nanoscale by using fundamental condensed-matter excitations such as plasmons and phonons that lead to spectral regions of ENZ behavior. Deep subwavelength films are known to support coupled surface modes—ENZ modes—at the frequency where the film's dielectric permittivity vanishes [13–15]. Here we propose a system whose spectral properties are controlled by the interaction between the ENZ modes of semiconductor nanolayers and multiple, distinct, dipole resonant systems. In particular, we consider ENZ modes that are strongly coupled to metamaterial (MM) resonators and *simultaneously* strongly coupled to semiconductor phonons or quantum-well intersubband transitions (ISTs). Such three-way coupling leads to double- and triple-polariton branches in transmission and reflection spectra.

Prior work has shown the realization of double-polariton branches by coupling MMs to quantum-well ISTs [16–23], ENZ modes [24,25], and optical phonons [26,27]. More generally, MM structures interacting with semiconductor heterostructures supporting excitations such as phonons, plasmons, and electronic transitions offer a platform for tunable spectral behavior that is attractive for low-voltage tunable filters [28], innovative efficient nonlinear elements [29–31], and light-emitting diodes [32]. Our objective here is to show the advantages of using ENZ modes for tailoring the spectral response of strongly coupled systems.

The platform discussed in this paper is represented by the block diagram in Fig. 1(a), which describes a platform where ENZ modes interact with two distinct dipole resonant systems. In this work, one of the resonant systems will always be MM resonators, while the other will be either semiconductor phonons or quantum-well ISTs. Note that both the ENZ mode and the ISTs require z-polarized fields, which are readily generated in the near field of the MM resonators. Of course, one can envision a more general system in which the ENZ modes interact with more than two dipole resonances, but the analysis provided here is sufficient to understand the achievable properties. In some cases, the ENZ mode and the second dipole resonance coexist in the same nanolayer, as happens in the case of semiconductor optical phonons shown in Fig. 1(b). This implementation is, however, limited by the inability to adjust the optical phonon frequency and the detuning between the ENZ mode and the phonon resonance. This limitation can be overcome by using two layers, one supporting the required ENZ modes and the other supporting the second dipole resonance as shown in Fig. 1(c) for the case of quantum-well ISTs. This is the most flexible case, in which the relative positions and resonance frequencies of the ENZ and dipole layers determine the complex spectral response of the strongly coupled system.

In what follows, we analyze three representative cases of three-way coupling using ENZ modes. In Sec. II, we examine as "case 1" the simultaneous strong coupling of ENZ modes to MM resonators and optical phonons, where

*sncampi@sandia.gov
†ibrener@sandia.gov

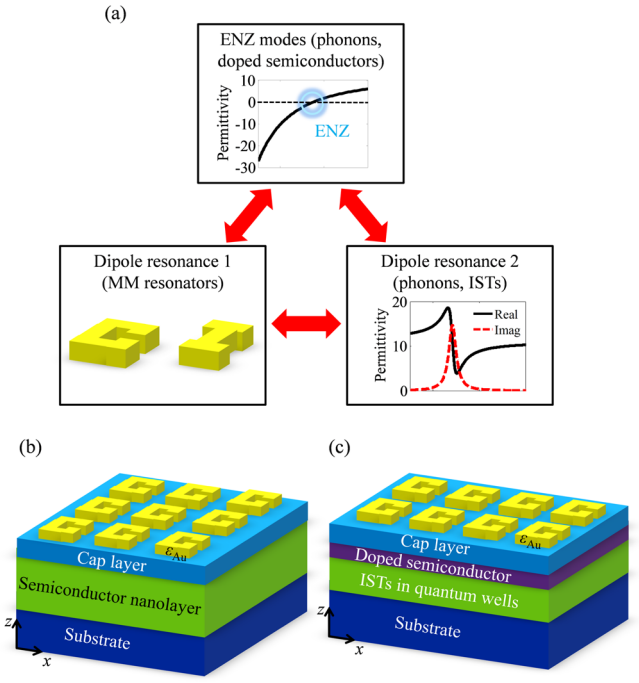

FIG. 1. ENZ modes arising from condensed-matter excitations such as phonons and plasmons represent a new path for tailoring light-matter interactions at the nanoscale. (a) Block diagram of the proposed platform comprising ENZ modes and two dipole resonances. The ENZ modes will be simultaneously coupled to MM resonators and a second resonant system which will either be (b) optical phonons occurring in the ENZ layer or (c) quantum-well ISTs occurring in a separate layer. MM resonators are shown on top of each semiconductor heterostructure in panels (b) and (c).

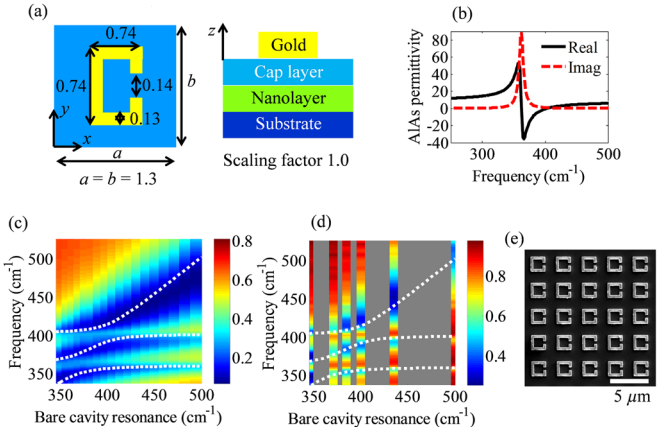

FIG. 2. Numerical and experimental results for strong coupling between MMs and optical phonons. (a) Top and side views of the structure with dimensions in micrometer for scaling factor 1.0. (b) Real and imaginary parts of the permittivity of undoped AlAs versus frequency. (c) Map of simulated transmittance versus the incident wave frequency and the bare cavity resonant frequency for a MM of gold split-ring resonators above the AlAs ENZ and phonon layer. Note the formation of three polariton branches. (d) Experimental transmittance spectra for several bare cavity resonant frequencies (i.e., scaling factors). Good agreement between numerical and experimental results is observed. The dotted lines representing the three polariton branches are shown as guides to the eye in panels (c) and (d). (e) SEM image of a MM sample with scaling factor 2.6 fabricated with electron-beam lithography.

we clearly observe the generation of three polariton branches. This is in contrast to the results of Ref. [26] where the polariton branch due to the ENZ mode was barely visible. In Sec. III, we investigate as "case 2" the strong coupling between the ENZ mode and quantum-well ISTs, for the case where the frequencies of the ENZ mode and ISTs are detuned. This case helps us unravel the physics of strong coupling with optical phonons. Finally, in Sec. IV we analyze as "case 3" the case where the frequencies of the ENZ modes and ISTs are degenerate.

II. CASE 1: SIMULTANEOUS STRONG COUPLING OF ENZ MODES TO MM RESONATORS AND OPTICAL PHONONS

In this section, we investigate the spectral properties of a system comprising 100-nm-thick gold split-ring-resonator MMs and a semiconductor heterostructure as in Fig. 2(a) containing a 3-nm-thick GaAs cap layer, a 10-nm-thick AlAs layer, and a GaAs substrate. The relative permittivity of gold $\varepsilon_{\mathrm{Au}}$ is described using a Drude model [33] with parameters extracted from spectral ellipsometry measurements of a 100-nm-thick gold film which yields a plasma angular frequency of $2\pi \times 2060 \times 10^{12}$ rad/s and a damping rate of $2\pi \times 10.9 \times 10^{12}$ rad/s. The AlAs nanolayer supports optical phonons at approximately 360 cm^{-1} [see Fig. 2(b)], and the ENZ region associated with this resonance occurs at approximately 400 cm^{-1}. Note that since the ENZ frequency arises as a result of the phonon resonance, its frequency is fixed for a given material, thus, providing limited capabilities with respect to the system analyzed in Secs. III and IV. Because of the spectral separation of the phonon and ENZ frequencies, we anticipate that both the phonons and the ENZ modes will strongly couple to the MMs and lead to polariton splitting. Note that the particular geometry used for the MM resonators is not important, so long as the bare cavity resonance is controlled by the size of the resonators.

Figure 2(c) shows the transmittance as a function of incident wave frequency and bare cavity resonance frequency obtained from full-wave simulations [34] of the split-ring-resonator array on top of the AlAs nanolayer. To generate the transmittance map in Fig. 2(c), we simulate a set of MMs for which all the spatial dimensions of the MM of split-ring resonators are scaled by a common scaling factor that varies between 2.0 and 2.9 relative to the dimensions shown in Fig. 2(a). For each scaling factor, we perform a full-wave simulation of the MM without the AlAs layer to determine the bare cavity resonance frequency as the location of minimum transmittance. Next, we perform simulations

including the AlAs nanolayer and plot the obtained transmittance spectra versus the bare cavity frequency. A similar procedure is used to generate all the full-wave simulation transmittance maps shown in this manuscript. We observe clearly that the transmittance spectra exhibit three polariton branches, a signature of strong coupling of the MM resonators to both the phonon resonance (around 360 cm^{-1}) and the ENZ mode (around 400 cm^{-1}).

Next, we experimentally verify the predictions of Fig. 2(c). Similar to the full-wave simulations, we geometrically scale the MM dimensions which allow us to sweep the bare cavity resonance across the ENZ and phonon resonance frequencies and map out the three polariton branches. The MM is defined by electron-beam lithography directly on top of the semiconductor heterostructure. A Ti/Au (5/100 nm) layer is evaporated followed by a standard lift-off process. A scanning-electron-micrograph (SEM) image of a fabricated sample is reported in Fig. 2(e). The transmittance spectra are measured at room temperature using a Bruker IFS 66v and are shown in Fig. 2(d). Two transparency windows, i.e., three polariton branches, are clearly visible at 360 and 400 cm^{-1} in agreement with full-wave simulations.

As mentioned earlier, the implementation presented in Fig. 2 is limited by the inability to adjust the optical phonon frequency and the detuning between the ENZ mode and the phonon resonance. In the next sections, we propose an alternative implementation to overcome this limitation.

III. CASE 2: FULLY ENGINEERABLE SYSTEM WITH DETUNED ENZ MODE AND IST FREQUENCIES

The results of Sec. II demonstrate that optical phonons can be utilized to tailor the behavior of photonic structures and open up new directions for their usage in strong-coupling scenarios. However, optical phonon frequencies are defined by intrinsic material properties and can hardly be modified. To circumvent this problem, we separate the functionality and use a doped semiconductor layer to create the ENZ modes, and a multi-quantum-well layer containing ISTs as the second dipole resonance. This system is fully tunable since the ENZ frequency can be adjusted by varying the doping level, and the IST frequencies can be tuned by modifying the quantum-well design. In particular, we adopt the structure shown in the inset of Fig. 3 which consists of a MM array of dog-bone resonators (gold, 100 nm thick) placed on top of a multilayered substrate comprising an $Al_{0.48}In_{0.52}As$ cap layer (30 nm thick) with $\varepsilon_c = 10.23$, a doped $In_{0.53}Ga_{0.47}As$ layer exhibiting an ENZ effect, a quantum-well slab containing 20 repeat units of an $In_{0.53}Ga_{0.47}As/Al_{0.48}In_{0.52}As$ heterostructure (12.5/20 nm) supporting ISTs at a frequency of approximately 24.2 THz, and an InP substrate with $\varepsilon_s = 9.3$. The relative permittivity of the doped InGaAs, ε_{ENZ} is described with a Drude model

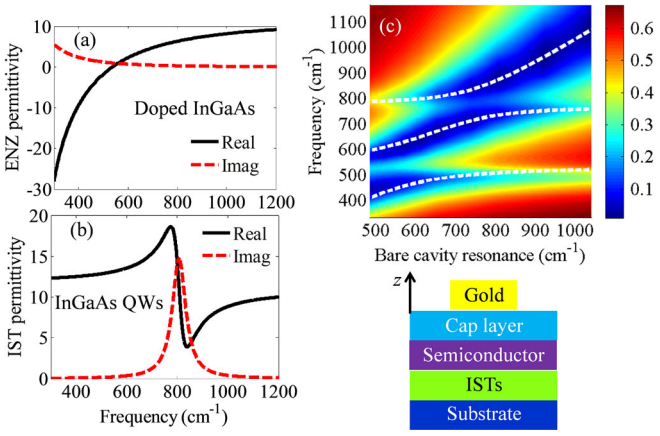

FIG. 3. Numerical results of strong coupling between MMs and detuned ENZ and IST frequencies. (a) Real and imaginary parts of the permittivity of doped InGaAs with the ENZ frequency at approximately 600 cm^{-1}. (b) Real and imaginary parts of the permittivity of InGaAs quantum wells with the IST dipole transition at approximately 800 cm^{-1}. (c) Transmittance map from full-wave simulations of gold dogbone resonators on top of a semiconductor heterostructure with detuned ENZ mode and IST transition frequencies. Note the formation of three polariton branches as in the case of optical phonons in Fig. 2. The dotted lines representing the three polariton branches are shown as guides to the eye. The inset shows the side view of the sample.

$$\varepsilon_{ENZ} = \varepsilon_\infty \left(1 - \frac{\omega_p^2}{\omega^2 + i\omega\gamma_{ENZ}}\right), \tag{1}$$

where ε_∞ is given by the Sellmeier equation for InGaAs, ω_p is the plasma frequency, and γ_{ENZ} is the damping rate. The monochromatic time harmonic convention $\exp(-i\omega t)$ is implicitly assumed. Since the plasma frequency is proportional to the doping density, the ENZ crossing point can be tuned by varying the doping density. The ISTs are described by anisotropic Lorentzian oscillators with (relative) dielectric tensor given as $\underline{\boldsymbol{\varepsilon}}_{IST} = \varepsilon_t(\hat{\mathbf{x}}\,\hat{\mathbf{x}} + \hat{\mathbf{y}}\,\hat{\mathbf{y}}) + \varepsilon_z\hat{\mathbf{z}}\,\hat{\mathbf{z}}$, with $\varepsilon_t = 10.97$ and

$$\varepsilon_z = \varepsilon_t + \frac{f_z\omega_0^2}{\omega_0^2 - \omega^2 - 2i\omega\gamma_{IST}}, \tag{2}$$

where $\omega_0 = 2\pi \times 24.2 \times 10^{12}$ rad/s is the IST angular frequency, $2\gamma_{IST}$ represents the IST damping rate, with $\gamma_{IST} = 2\pi \times 10^{12}$ rad/s, and $f_z = 1.2$ is proportional to the IST oscillator strength, the doping density, and intersubband matrix elements as described in Ref. [23].

In this section, we analyze the case where the ENZ mode frequency (approximately 600 cm^{-1}) is detuned from the IST transition frequency (approximately 800 cm^{-1}). The permittivities of the two layers are shown in Figs. 3(a) and 3(b), which clearly show the ENZ crossing and the IST resonance, respectively. Figure 3(c) shows the transmittance maps obtained from full-wave simulations of an array

of dogbone resonators on top of a doped semiconductor layer and a multi-quantum-well layer as a function of the bare cavity resonance. We observe clearly that the transmittance spectra exhibit three polariton branches, a signature of strong coupling of the MM resonators to an ENZ mode (around 600 cm^{-1}) that is detuned from the ISTs (around 800 cm^{-1}). This is very similar to what we observe in Fig. 2 for MMs strongly coupled to optical phonons supported by semiconductor nanolayers.

As mentioned earlier, the implementation presented in Fig. 3 is fully engineerable; i.e., the resonance frequencies of the ENZ and dipole layers can be adjusted independently. We further analyze this property in the next section.

IV. CASE 3: FULLY ENGINEERABLE SYSTEM WITH OVERLAPPING ENZ MODE AND IST FREQUENCIES

A more interesting effect is achieved using the MM-ENZ-IST structure in the inset of Fig. 3 when the doping of the ENZ layer is increased so that the frequency of the ENZ mode coincides with the ISTs resonant frequency (approximately 800 cm^{-1}) [see Fig. 4(a), which clearly shows the ENZ crossing at approximately 800 cm^{-1}]. We analyze this system for three thicknesses of the ENZ layer (the quantum-well thickness is kept constant). The resulting simulated transmittance maps for the three cases are shown in Figs. 4(b)–(d), which reveal that *only two polariton branches* are present in this configuration. This is in stark contrast to the three polariton branches observed in Fig. 3(c) for detuned ENZ mode and IST resonance frequencies. We find that the MM-ENZ-IST system exhibits a larger Rabi splitting than when the MM resonators are only coupled to the ENZ mode or the ISTs. Furthermore, Fig. 4(e) shows that the Rabi splitting increases as the thickness of the ENZ layer increases.

The increase of the Rabi splitting with increasing ENZ layer thickness for the combined ENZ layer and IST layer can be understood by considering the dispersion of the ENZ modes of this combined stack [shown in Fig. 5(a)]. Here we analyze a stack consisting of a doped $In_{0.53}Ga_{0.47}As$ layer with a plasma frequency at approximately 800 cm^{-1}, a

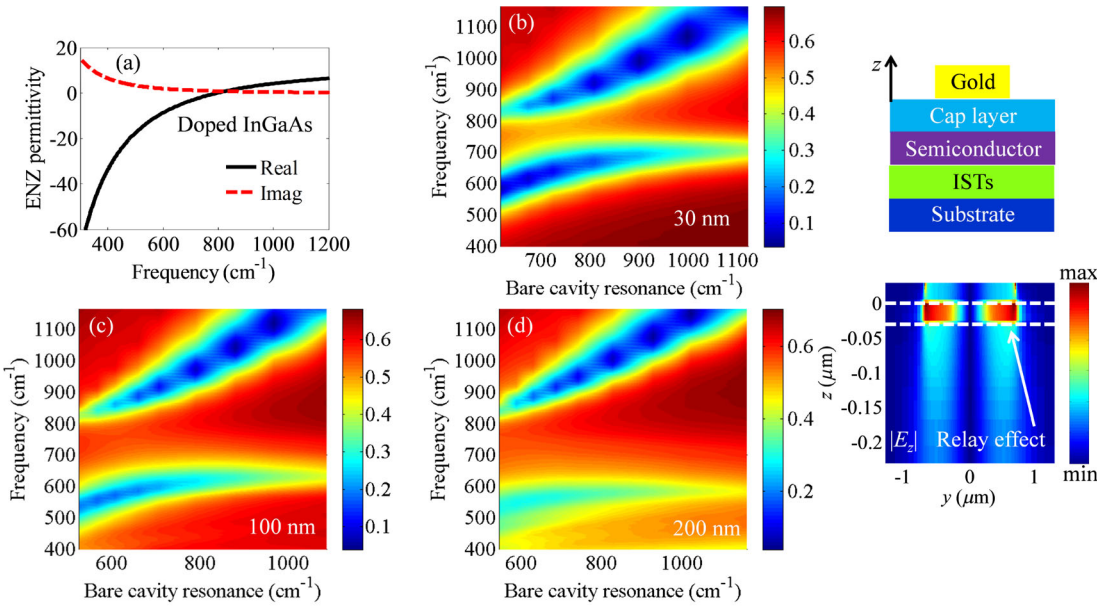

(e)

	IST only	ENZ only 30 nm	ENZ only 100 nm	ENZ only 200 nm	ENZ 30 nm and 651 nm IST	ENZ 100 nm and 651 nm IST	ENZ 200 nm and 651 nm IST
Theory	150	177	250	280	240	300	315
Exp	120	180	NA	NA	NA	320	340

FIG. 4. Numerical results of strong coupling in the MM-ENZ-IST system for the case of degenerate ENZ and IST frequencies. (a) Real and imaginary parts of the permittivity of doped InGaAs with the ENZ crossing at approximately 800 cm^{-1}. (b)–(d) Full-wave simulation transmittance maps for an array of dogbone resonators on top of a semiconductor heterostructure with overlapping ENZ mode and IST resonance frequencies for ENZ layer thicknesses of (b) 30 nm, (c) 100 nm, and (d) 200 nm. The inset shows the side view of the sample and $|Ez|$ field relay effect. (e) Experimental and theoretical values for the Rabi splitting in cm^{-1} (as the spectral difference between the two transmittance dips when the resonances are all overlapping) versus strong-coupling configuration: IST only, ENZ only, and both IST and ENZ. The last always shows the largest splitting.

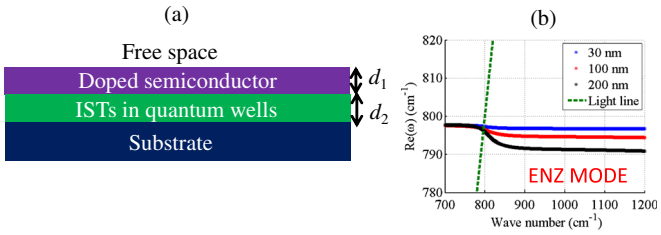

FIG. 5. (a) Semiconductor heterostructure for which we compute the dispersion of the ENZ modes. (b) Real part of the ENZ mode dispersions for the semiconductor heterostructures in (a) with ENZ layer thicknesses of 30, 100, and 200 nm. Note the relatively flat dispersion of Re(ω) versus wave number for all the ENZ layer thicknesses.

quantum-well slab supporting ISTs at a frequency of approximately 800 cm^{-1}, and an InP substrate. We compute the dispersion of the modes in the complex-frequency—real-wave-number plane and show it in Fig. 5(b). One can see that for the three ENZ layer thicknesses considered, the modes of the combined stack exhibit a rather flat dependence on the wave number, confirming that they behave as ENZ modes similar to those of a single slab [13–15]. This result, in turn, shows that the semiconductor stack in Fig. 5(a) effectively behaves as a "*thicker*" ENZ structure, leading to an enhanced Rabi splitting. A similar effect was used in Ref. [25] to obtain ultrastrong coupling thanks to a complete overlap between the photon mode and the matter polarization. A similar Rabi splitting increase with thickness was also observed in Ref. [35].

We also note that the ENZ mode plays a fundamental role in these effects: while, in general, the enhanced field generated below the paddles of the dogbone resonators decays exponentially with distance away from the metamaterial resonators, a thin layer supporting the ENZ modes acts as a *relayer* of E_z fields [13–15]. Because of boundary conditions of the ENZ layer, the field is enhanced and kept constant within the ENZ layer [13–15], so that it is relayed from the top interface to the bottom interface. This field-relay effect can clearly be seen in the inset of Fig. 4, which shows the $|E_z|$ in the y-z plane at 1000 cm^{-1} for the sample of Fig. 4(b) with scaling factor 1.0. The top and bottom interfaces of the ENZ layer are depicted by white dashed lines in this figure. On these grounds, we note that the use of an ENZ layer is beneficial as it helps alleviate the field penetration depth limitations mentioned in Ref. [20], provided the overall thickness is within the existence condition of ENZ modes [13–15]. Therefore, the best strategy to maximize the Rabi splitting in a metasurface–semiconductor system is to use a combination of a doped layer supporting an ENZ feature and a layer supporting ISTs, with overlapping ENZ and IST frequencies.

To confirm the predictions of Figs. 4(c) and 4(d), we fabricated MM samples for ENZ layer thicknesses of 100 and 200 nm. Figure 6 shows a SEM image of a MM for the 200-nm case and for a MM scaling factor 1.3, along with an

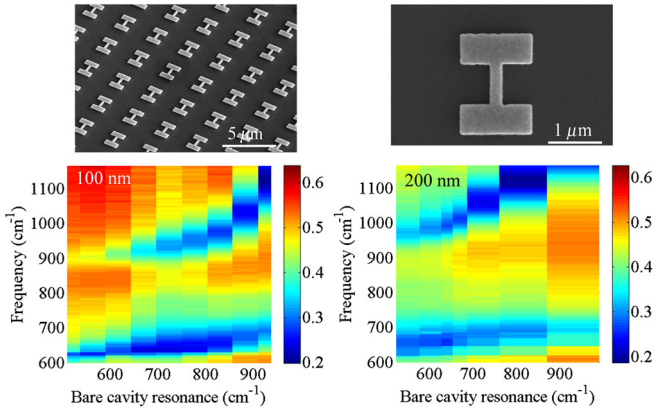

FIG. 6. Experimental transmittance maps for strong coupling in the MM-ENZ-IST system for degenerate ENZ and IST frequencies, with ENZ layer thicknesses of 100 and 200 nm. Note the good agreement between experimental data and simulation results in Figs. 4(c) and 4(d). The insets show SEM images of a MM sample and a single resonator fabricated with electron-beam lithography.

image of a single dogbone resonator. The experimental transmittance maps of the two samples are shown in Fig. 6. As predicted in Figs. 4(c) and 4(d), we obtain only two polariton branches and a large Rabi splitting. The minor disagreement between the simulations and measurements can be attributed to fabrication imperfections.

V. CONCLUSION

In conclusion, we demonstrate a platform for tailoring light-matter interactions that employs fundamental excitations in condensed matter such as plasmons and phonons. In particular, we design the system's spectral response by creating ENZ modes in semiconductor nanolayers and controlling their interaction with multiple, distinct dipole resonant systems. We show examples of this behavior for three-way strongly coupled systems of ENZ modes, phonons, and metamaterials, as well as three-way systems of ENZ modes, quantum-well ISTs, and metamaterials. The three-way coupling in these systems results in double- and triple-polariton branches in transmission spectra. In regards to the double-polariton branch case, we find that the best strategy to maximize the Rabi splitting is to use a combination of a doped layer supporting an ENZ feature and a layer supporting ISTs, with overlapping ENZ and IST frequencies. The flexibility of tuning resonance frequencies and couplings renders this platform attractive for low-voltage tunable filters, light-emitting diodes, and efficient nonlinear composite materials.

ACKNOWLEDGMENTS

The authors acknowledge fruitful discussions with Professor Francois Marquier, Institut d'Optique, France. This work is supported by the U.S. Department of Energy, Office of Basic Energy Sciences, Division of Materials

Sciences and Engineering and performed, in part, at the Center for Integrated Nanotechnologies, an Office of Science User Facility operated for the U.S. Department of Energy Office of Science. Sandia National Laboratories is a multiprogram laboratory managed and operated by Sandia Corporation, a wholly owned subsidiary of Lockheed Martin Corporation, for the U.S. Department of Energy's National Nuclear Security Administration under Contract No. DE-AC04-94AL85000.

S. C. and S. L. contributed equally to this work and are joint first authors.

[1] N. Engheta, Pursuing near-zero response, Science **340**, 286 (2013).

[2] M. Silveirinha and N. Engheta, Tunneling of Electromagnetic Energy Through Subwavelength Channels and Bends Using ε-Near-Zero Materials, Phys. Rev. Lett. **97**, 157403 (2006).

[3] R. Liu, Q. Cheng, T. Hand, J. J. Mock, T. J. Cui, S. A. Cummer, and D. R. Smith, Experimental Demonstration of Electromagnetic Tunneling Through an Epsilon-Near-Zero Metamaterial at Microwave Frequencies, Phys. Rev. Lett. **100**, 023903 (2008).

[4] D. C. Adams, S. Inampudi, T. Ribaudo, D. Slocum, S. Vangala, N. A. Kuhta, W. D. Goodhue, V. A. Podolskiy, and D. Wasserman, Funneling Light Through a Subwavelength Aperture with Epsilon-Near-Zero Materials, Phys. Rev. Lett. **107**, 133901 (2011).

[5] K. C. Gupta, Narrow-beam antennas using an artificial dielectric medium with permittivity less than unity, Electron. Lett. **7**, 16 (1971).

[6] S. Enoch, G. Tayeb, P. Sabouroux, N. Guérin, and P. Vincent, A Metamaterial for Directive Emission, Phys. Rev. Lett. **89**, 213902 (2002).

[7] G. Lovat, P. Burghignoli, F. Capolino, D. R. Jackson, and D. R. Wilton, Analysis of directive radiation from a line source in a metamaterial slab with low permittivity, IEEE Trans. Antennas Propag. **54**, 1017 (2006).

[8] A. Alù, M. G. Silveirinha, A. Salandrino, and N. Engheta, Epsilon-near-zero metamaterials and electromagnetic sources: Tailoring the radiation phase pattern, Phys. Rev. B **75**, 155410 (2007).

[9] N. Engheta, Circuits with light at nanoscales: Optical nanocircuits inspired by metamaterials, Science **317**, 1698 (2007).

[10] C. Argyropoulos, P.-Y. Chen, G. D'Aguanno, N. Engheta, and A. Alù, Boosting optical nonlinearities in ε-near-zero plasmonic channels, Phys. Rev. B **85**, 045129 (2012).

[11] D. de Ceglia, S. Campione, M. A. Vincenti, F. Capolino, and M. Scalora, Low-damping epsilon-near-zero slabs: Nonlinear and nonlocal optical properties, Phys. Rev. B **87**, 155140 (2013).

[12] A. Monti, F. Bilotti, A. Toscano, and L. Vegni, Possible implementation of epsilon-near-zero metamaterials working at optical frequencies, Opt. Commun. **285**, 3412 (2012).

[13] S. Vassant, J. P. Hugonin, F. Marquier, and J. J. Greffet, Berreman mode and epsilon near zero mode, Opt. Express **20**, 23971 (2012).

[14] S. Vassant, A. Archambault, F. Marquier, F. Pardo, U. Gennser, A. Cavanna, J. L. Pelouard, and J. J. Greffet, Epsilon-Near-Zero Mode for Active Optoelectronic Devices, Phys. Rev. Lett. **109**, 237401 (2012).

[15] S. Campione, I. Brener, and F. Marquier, Theory of epsilon-near-zero modes in ultrathin films, Phys. Rev. B **91**, 121408 (2015).

[16] P. Jouy, A. Vasanelli, Y. Todorov, A. Delteil, G. Biasiol, L. Sorba, and C. Sirtori, Transition from strong to ultrastrong coupling regime in mid-infrared metal-dielectric-metal cavities, Appl. Phys. Lett. **98**, 231114 (2011).

[17] A. Delteil, A. Vasanelli, Y. Todorov, C. Feuillet Palma, M. Renaudat St-Jean, G. Beaudoin, I. Sagnes, and C. Sirtori, Charge-Induced Coherence between Intersubband Plasmons in a Quantum Structure, Phys. Rev. Lett. **109**, 246808 (2012).

[18] G. Scalari, C. Maissen, D. Hagenmuller, S. De Liberato, C. Ciuti, C. Reichl, W. Wegscheider, D. Schuh, M. Beck, and J. Faist, Ultrastrong light-matter coupling at terahertz frequencies with split ring resonators and inter-Landau level transitions, J. Appl. Phys. **113**, 136510 (2013).

[19] D. Dietze, A. Benz, G. Strasser, K. Unterrainer, and J. Darmo, Terahertz meta-atoms coupled to a quantum well intersubband transition, Opt. Express **19**, 13700 (2011).

[20] A. Benz, S. Campione, S. Liu, I. Montaño, J. F. Klem, A. Allerman, J. R. Wendt, M. B. Sinclair, F. Capolino, and I. Brener, Strong coupling in the sub-wavelength limit using metamaterial nanocavities, Nat. Commun. **4**, 2882 (2013).

[21] S. Campione, A. Benz, J. F. Klem, M. B. Sinclair, I. Brener, and F. Capolino, Electrodynamic modeling of strong coupling between a metasurface and intersubband transitions in quantum wells, Phys. Rev. B **89**, 165133 (2014).

[22] A. Gabbay and I. Brener, Theory and modeling of electrically tunable metamaterial devices using inter-subband transitions in semiconductor quantum wells, Opt. Express **20**, 6584 (2012).

[23] A. Gabbay, J. Reno, J. R. Wendt, A. Gin, M. C. Wanke, M. B. Sinclair, E. Shaner, and I. Brener, Interaction between metamaterial resonators and intersubband transitions in semiconductor quantum wells, Appl. Phys. Lett. **98**, 203103 (2011).

[24] Y. C. Jun, J. Reno, T. Ribaudo, E. Shaner, J.-J. Greffet, S. Vassant, F. Marquier, M. Sinclair, and I. Brener, Epsilon-near-zero strong coupling in metamaterial-semiconductor hybrid structures, Nano Lett. **13**, 5391 (2013).

[25] B. Askenazi, A. Vasanelli, A. Delteil, Y. Todorov, L. C. Andreani, G. Beaudoin, I. Sagnes, and C. Sirtori, Ultra-strong light–matter coupling for designer Reststrahlen band, New J. Phys. **16**, 043029 (2014).

[26] D. J. Shelton, I. Brener, J. C. Ginn, M. B. Sinclair, D. W. Peters, K. R. Coffey, and G. D. Boreman, Strong coupling between nanoscale metamaterials and phonons, Nano Lett. **11**, 2104 (2011).

[27] F. Neubrech, D. Weber, D. Enders, T. Nagao, and A. Pucci, Antenna sensing of surface phonon polaritons, J. Phys. Chem. C **114**, 7299 (2010).

[28] A. Benz, I. Montano, J. F. Klem, and I. Brener, Tunable metamaterials based on voltage controlled strong coupling, Appl. Phys. Lett. **103**, 263116 (2013).

[29] S. Campione, A. Benz, M. B. Sinclair, F. Capolino, and I. Brener, Second harmonic generation from metamaterials strongly coupled to intersubband transitions in quantum wells, Appl. Phys. Lett. **104**, 131104 (2014).

[30] J. Lee, M. Tymchenko, C. Argyropoulos, P.-Y. Chen, F. Lu, F. Demmerle, G. Boehm, M.-C. Amann, A. Alu, and M. A. Belkin, Giant nonlinear response from plasmonic metasurfaces coupled to intersubband transitions, Nature (London) **511**, 65 (2014).

[31] O. Wolf, S. Campione, A. Benz, A. P. Ravikumar, S. Liu, T. S. Luk, E. A. Kadlec, E. A. Shaner, J. F. Klem, M. B. Sinclair, and I. Brener, Phased-array sources based on nonlinear metamaterial nanocavities, Nat. Commun. **6**, 7667 (2015).

[32] M. Geiser, G. Scalari, F. Castellano, M. Beck, and J. Faist, Room temperature terahertz polariton emitter, Appl. Phys. Lett. **101**, 141118 (2012).

[33] M. A. Ordal, L. L. Long, R. J. Bell, S. E. Bell, R. R. Bell, J. R. W. Alexander, and C. A. Ward, Optical properties of the metals Al, Co, Cu, Au, Fe, Pb, Ni, Pd, Pt, Ag, Ti, and W in the infrared and far infrared, Appl. Opt. **22**, 1099 (1983).

[34] FDTD Solutions by FDTD Lumerical Inc., https://www.lumerical.com/.

[35] A. Benz, S. Campione, S. Liu, I. Montano, J. F. Klem, M. B. Sinclair, F. Capolino, and I. Brener, Monolithic metallic nanocavities for strong light-matter interaction to quantum-well intersubband excitations, Opt. Express **21**, 32572 (2013).